Nonlinear inversion of seismic amplitude data for attenuation and layer-weaknesses

Huaizhen Chen* and Kristopher A. Innanen

ABSTRACT

Based on a model of periodically layered media, we first express frequency-dependent stiffness parameters in terms of P-wave attenuation factor and lay-weaknesses. Using perturbations in frequency-dependent stiffness parameters for an interface separating two periodically layered media, we derive a linearized P-to-P reflection coefficient as a function of layer-weaknesses and P-wave attenuation factor, from which an expression of anisotropic and anelastic impedance is proposed. In order to estimate layer-weaknesses and P-wave attenuation factor, we first utilize a model-based damped least-squares inversion approach to estimate the anisotropic and anelastic impedances from frequency-components of partially-stacked seismic data. Using the estimated anisotropic and anelastic impedances, we implement nonlinear inversion for unknown parameter vector (P- and S-wave moduli, density, layer-weaknesses and P-wave attenuation factor), in which Bayesian Markov chain Monte Carlo algorithm is employed. Synthetic tests confirm that the unknown parameter vector involving P- and S-wave moduli, density, layer-weaknesses and P-wave attenuation factor is estimated stably and reliably in the case of signal-to-noise ratio of 2. Applying the inversion approach to a field data set, we observe that reliable results of layer-weaknesses and P-wave attenuation factor are obtained. We conclude that the proposed inversion approach may provide additional proofs for reservoir characterization and fluid identification.

INTRODUCTION

Seismic waves exhibit anisotropy and attenuation characteristics when propagating in underground porous and cracked layers. Many studies focus on anisotropy features of seismic wave propagation that are induced by thin layers of sediments (Thomsen, 1986; Alkhalifah and Tsvankin, 1995; Tsvankin, 1996), which is considered as vertically transverse isotropy (VTI), and anisotropic features that are caused by vertical or sub-vertical fractures (Tsvankin, 1997; Rüger and Tsvankin, 1997; Bakulin et al., 2000), which is known as horizontally transverse isotropy (HTI). Attenuation of seismic wave, which is caused by fluid movement between pores and fractures when wave passing the rock (known as wave-induced fluid flow, WIFF), have been well studied in the aspect of seismic rock physics (Chapman, 2003; Gurevich et al., 2009; Müller et al., 2010). A periodically layered model for studying P-wave attenuation in porous and fractured media is proposed by Brajanovski et al. (2005), which mainly consists of a thin fractured layer and a thick porous background layer. Based on the periodically layered model, stiffness parameters of anisotropic and anelastic rocks, which consider both effect of fractures and pores can be expressed (Guo et al., 2018; Chen and Innanen, 2018).

Seismic reflection coefficients expressed in terms of variables sensitive to anisotropy or attenuation are important for both seismic forward modeling and seismic data inversion. Thomsen (1986) presents weak anisotropy parameters. Rüger (1998) derives PP- and PS-wave reflection coefficients in terms of weak anisotropy parameters and new modified

anisotropy parameters. Using a scattering model, Shaw and Sen (2004) assume stiffness parameters of anisotropic rocks to be the sum of isotropic background stiffness parameters and anisotropy-induced perturbations, and they propose a relationship between reflection coefficients and scattering potentials that are related to anisotropy-induced perturbations. For analyzing effect of attenuation on seismic wave reflection response, Borcherdt (2009) theoretically describes how plane waves reflect and refract at viscoelastic boundaries in the condition of the constant quality factor Q model. Assuming attenuation to be perturbation in elastic properties (e.g. velocity and moduli), Moradi and Innanen (2015) derive scattering of seismic waves in viscoelastic media, and Moradi and Innanen (2016) express complex PP- and PS-wave reflection coefficients under the assumption of constant Q model; however, the attenuation factors appear in the imaginary parts of the derived reflection coefficients. Combining attenuation factor computed using the squirt model proposed by Mavko and Jizba (1991) and Dvorkin and Mavko (2006), and wave velocity defined by Aki and Richards (2002) in anelastic media, Chen et al. (2018a) derive a frequency-dependent PP-wave reflection coefficient as a function of P- and S-wave attenuation factors ($1/Q_{\rm P}$ and $1/Q_{\rm S}$), and the attenuation factors exhibit in both real and imaginary parts of reflection coefficient. In order to model seismic reflection characteristics in anisotropic and anelastic media, a frequency-dependent reflection coefficient that considers both effects of anisotropy and attenuation, should be derived.

Estimation of anisotropy and attenuation has become an important part of reservoir characterization. seismic inversion for VTI media focuses on employing seismic data of relatively large offset to estimate weak anisotropy parameters (Rüger, 1998; Grechka et al., 2002); for HTI media, amplitude variation with offset and azimuth (AVOAz) data are utilized for estimating variables sensitive to fractures, e.g., azimuthal seismic inversion for fracture weaknesses and compliances (Downton and Roure, 2010, 2015; Chen et al., 2017, 2018b). Amplitude-variation with frequency data are employed to predict attenuation factor $1/Q$ based on the derived frequency-dependent reflection coefficient (Innanen, 2011; Bird, 2012). Chen et al. (2018a) propose an inversion approach of employing frequency components of seismic data to estimate P- and S-wave attenuation factors based on anelastic impedance. In the present study, we first express simplified stiffness parameters in terms of lay-weaknesses and attenuation factor based the periodically layered model. Using perturbations in stiffness parameters, we derive an approximate frequency-dependent reflection coefficient and anisotropic anelastic impedance ($\mathcal{A}_{\rm EI}$) as a function of attenuation factor and layer-weaknesses. Based on the reflection coefficient and anelastic impedance, we establish an inversion approach and workflow of employing frequency-components extracted from seismic data to estimate unknown parameters involving P- and S-wave moduli, density, attenuation factor and layer-weaknesses. Noisy synthetic seismic data are utilized to testify the stability and robustness of the proposed inversion approach; and applying the inversion approach and workflow to real data sets, we generate reliable results of attenuation factors and layer-weaknesses, which may be used as good indicators of reservoir prediction.

THEORY AND METHOD

In this section we will propose simplified stiffness parameters as functions of attenuation factors and weaknesses for periodically layered media that are constructed by a com-

pliance layer and a stiff porous layer, as plotted in Figure 1. We stress that in the present study we assume the weaknesses are mainly induced by the compliant layer and attenuation are caused by wave-induced fluid flow (WIFF) in the stiff porous layer when seismic wave propagates in the media. Using the simplified stiffness parameters, we will derive

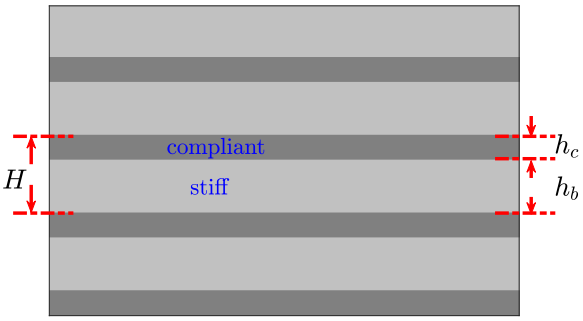

FIG. 1. Periodically layered media. The quantities $h_{\rm c}$ and $h_{\rm b}$ represent thicknesses of compliant and stiff layers, and $H = h_{\rm c} + h_{\rm b}$.

a linearized P-to-P reflection coefficient, which involves effects of elastic parameters (e.g. P- and S-wave moduli), attenuation factors (i.e. inverse quality factors) and weaknesses. Based on the proposed reflection coefficient, we will establish an approach and workflow of employing observed seismic data to estimate elastic parameters, attenuation factors and weaknesses.

Simplification of frequency-dependent stiffness parameters

We first propose how to simplify stiffness parameters for periodically layered media. Stiffness matrix of periodically layered media is given by Backus (1962) and Carcione (2015), which is the same to the stiffness matrix of vertical transversely isotropic (VTI) media

$$\mathbf{C} = \begin{bmatrix} C_{11} & C_{12} & C_{13} & 0 & 0 & 0 \\ C_{12} & C_{11} & C_{13} & 0 & 0 & 0 \\ C_{13} & C_{13} & C_{33} & 0 & 0 & 0 \\ 0 & 0 & 0 & C_{55} & 0 & 0 \\ 0 & 0 & 0 & 0 & C_{55} & 0 \\ 0 & 0 & 0 & 0 & 0 & C_{66} \end{bmatrix}, \tag{1}$$

where

$$C_{11} = \frac{H^2 \mathcal{M}_{\rm c}\mathcal{M}_{\rm b} + 4h_{\rm c}h_{\rm b}\left(\mathcal{U}_{\rm c} - \mathcal{U}_{\rm b}\right)\left(\mathcal{M}_{\rm c} - \mathcal{U}_{\rm c} - \mathcal{M}_{\rm b} + \mathcal{U}_{\rm b}\right)}{H\left(h_{\rm c}\mathcal{M}_{\rm b} + h_{\rm b}\mathcal{M}_{\rm c}\right)},$$

$$C_{12} = \frac{H(\mathcal{M}_{\rm c} - 2\mathcal{U}_{\rm c})\left(\mathcal{M}_{\rm b} - 2\mathcal{U}_{\rm b}\right)}{h_{\rm c}\mathcal{M}_{\rm b} + h_{\rm b}\mathcal{M}_{\rm c}} + \frac{2\left[\left(\mathcal{M}_{\rm c} - 2\mathcal{U}_{\rm c}\right)h_{\rm c} + \left(\mathcal{M}_{\rm b} - 2\mathcal{U}_{\rm b}\right)h_{\rm b}\right]\left(\mathcal{U}_{\rm b}h_{\rm c} + \mathcal{U}_{\rm c}h_{\rm b}\right)}{H\left(h_{\rm c}\mathcal{M}_{\rm b} + h_{\rm b}\mathcal{M}_{\rm c}\right)},$$

$$C_{13} = \frac{\left(\mathcal{M}_{\rm c} - 2\mathcal{U}_{\rm c}\right)h_{\rm c}\mathcal{M}_{\rm b} + \left(\mathcal{M}_{\rm b} - 2\mathcal{U}_{\rm b}\right)h_{\rm b}\mathcal{M}_{\rm c}}{h_{\rm c}\mathcal{M}_{\rm b} + h_{\rm b}\mathcal{M}_{\rm c}},$$

$$C_{33} = \frac{H\mathcal{M}_{\rm c}\mathcal{M}_{\rm b}}{h_{\rm c}\mathcal{M}_{\rm b} + h_{\rm b}\mathcal{M}_{\rm c}},$$

$$C_{55} = \frac{H\mathcal{U}_{\rm c}\mathcal{U}_{\rm b}}{h_{\rm c}\mathcal{U}_{\rm b} + h_{\rm b}\mathcal{U}_{\rm c}},$$
$$C_{66} = \frac{h_{\rm c}\mathcal{U}_{\rm c} + h_{\rm b}\mathcal{U}_{\rm b}}{H}, \tag{2}$$

in which $\mathcal{M}_{\rm c}$ and $\mathcal{M}_{\rm b}$ are P-wave complex moduli of compliant and stiff layers, $\mathcal{U}_{\rm c}$ and $\mathcal{U}_{\rm b}$ are S-wave complex moduli of compliant and stiff layers, $H = h_{\rm c} + h_{\rm b}$, $h_{\rm c}$ and $h_{\rm b}$ are thicknesses of compliant and stiff layers, respectively.

Following Brajanovski et al. (2005), we focus on the case of the limit $\frac{h_{\rm c}}{H} \to 0$ and setting $\frac{h_{\rm b}}{H}$ to 1; and involving definitions of excess normal and tangential compliances,

$$\lim_{h_{\rm c}\to 0} \frac{h_{\rm c}}{H\mathcal{M}_{\rm c}} \equiv Z_{\rm N},$$
$$\lim_{h_{\rm c}\to 0} \frac{h_{\rm c}}{H\mathcal{U}_{\rm c}} \equiv Z_{\rm T}, \tag{3}$$

and extending P- and S-wave moduli to be frequency-dependent we obtain simplified stiffness parameters

$$C_{11} \approx \mathcal{M}_{\rm b}\left[1 - (1-2\kappa_{\rm b})^2\,\delta_{\rm N}\right],$$
$$C_{12} \approx \mathcal{M}_{\rm b}(1-2\kappa_{\rm b})\left[1 - (1-2\kappa_{\rm b})\,\delta_{\rm N}\right],$$
$$C_{13} \approx \mathcal{M}_{\rm b}\,(1-2\kappa_{\rm b})\,(1-\delta_{\rm N}),$$
$$C_{33} \approx \mathcal{M}_{\rm b}\,(1-\delta_{\rm N}),$$
$$C_{55} \approx \mathcal{U}_{\rm b}\,(1-\delta_{\rm T}),$$
$$C_{66} \approx \mathcal{U}_{\rm b}, \tag{4}$$

where $\delta_{\rm N} = \frac{\mathcal{M}_{\rm b} Z_{\rm N}}{1+\mathcal{M}_{\rm b} Z_{\rm N}}$ and $\delta_{\rm T} = \frac{\mathcal{U}_{\rm b} Z_{\rm T}}{1+\mathcal{U}_{\rm b} Z_{\rm T}}$ are the normal and tangential layer weaknesses defined by Hsu and Schoenberg (1993), and $\kappa_{\rm b} = \frac{\mathcal{U}_{\rm b}}{\mathcal{M}_{\rm b}}$.

As we stress that the attenuation is mainly induced by WIFF in the porous background layer, we extend the simplified stiffness parameters to be frequency-dependent by involving the effect of attenuation factor into P- and S-wave moduli. In the present study, we focus on the case of 2D stiffness tensor of VTI media and employ definitions of frequency-dependent P- and S-wave moduli proposed by Chen et al. (2018a) to obtain the frequency-dependent stiffness parameters

$$C_{11} \approx M\left[1 + \frac{2\Gamma_f}{Q_{\rm P}} - (1-2\kappa)^2\,\delta_{\rm N}\right],$$
$$C_{13} \approx \lambda\left[1 + \frac{2\Gamma_f}{Q_{\rm P}} - \delta_{\rm N}\right],$$
$$C_{33} \approx M\left[1 + \frac{2\Gamma_f}{Q_{\rm P}} - \delta_{\rm N}\right],$$

$$C_{55} \approx \mu \left[1 + \frac{2\xi \Gamma_f}{Q_{\mathrm{P}}} - \delta_{\mathrm{T}} \right], \tag{5}$$

where $\lambda = M\,(1-2\kappa)$, $\Gamma_f = \frac{1}{\pi} \frac{2f/f_{\mathrm{r}}}{1+(f/f_{\mathrm{r}})^2} \log\left(\frac{f}{f_{\mathrm{r}}}\right)$, $\xi = \frac{4\kappa(1-\kappa)}{(1-2\kappa)^2(3-2\kappa)}$, $\kappa = \mu/M$, M and μ are elastic properties of background porous media at the reference frequency f_{r}, and $\frac{1}{Q_{\mathrm{P}}}$ is P-wave attenuation factor at the reference frequency f_{r} (Chen et al., 2018a).

Derivation of linearized and frequency-dependent P-to-P reflection coefficient and anelastic impedance

Using the derived simplified frequency-dependent stiffness parameters, we proceed to the derivation of P-to-P reflection coefficient for an interface separating two periodically layered layers as shown in Figure 2. Based on the perturbation theory, we assume the upper layer to be the reference medium, which is characterized by three elastic parameters (P-wave modulus M, S-wave modulus μ and density ρ), two layer-weakness parameters (δ_{N} and δ_{T}), and one attenuation factor (P-wave inverse quality factor $\frac{1}{Q_{\mathrm{P}}}$). Perturbations exhibit in the lower layer, which are expressed as $\left(\Delta M, \Delta\mu, \Delta\rho, \Delta\delta_{\mathrm{N}}, \Delta\delta_{\mathrm{T}}, \Delta\frac{1}{Q_{\mathrm{P}}}\right)$.

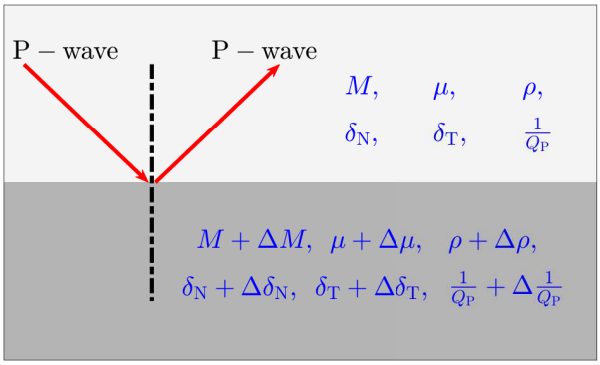

FIG. 2. An interface separating two periodically layered media.

Peturbation in stiffness matrix $\Delta\mathbf{C}$ is expressed as

$$\Delta\mathbf{C} = \begin{bmatrix} \Delta C_{11} & \Delta C_{13} & 0 \\ \Delta C_{13} & \Delta C_{33} & 0 \\ 0 & 0 & \Delta C_{55} \end{bmatrix}, \tag{6}$$

and using the derived stiffness parameters shown in equation 5, we express perturbations in the stiffness parameters as:

$$\Delta C_{11} \approx \Delta M + 2\Gamma_f M \Delta\frac{1}{Q_{\mathrm{P}}} - (1-2\kappa)^2 M \Delta\delta_{\mathrm{N}},$$

$$\Delta C_{13} \approx \Delta M - 2\Delta\mu + 2\Gamma_f (1-2\kappa) M \Delta\frac{1}{Q_{\mathrm{P}}} - (1-2\kappa) M \Delta\delta_{\mathrm{N}},$$

$$\Delta C_{33} \approx \Delta M + 2\Gamma_f M \Delta\frac{1}{Q_{\mathrm{P}}} - M \Delta\delta_{\mathrm{N}},$$

$$\Delta C_{55} \approx \Delta\mu + 2\xi \Gamma_f \mu \Delta \frac{1}{Q_{\mathrm{P}}} - \mu \Delta \delta_{\mathrm{T}}, \tag{7}$$

in which we neglect terms that are proportional to $\frac{1}{Q_{\mathrm{P}}}\Delta M$, $\Delta\frac{1}{Q_{\mathrm{P}}}\Delta M$, $\frac{1}{Q_{\mathrm{P}}}\Delta\mu$, $\Delta\frac{1}{Q_{\mathrm{P}}}\Delta\mu$, $\delta_{\mathrm{N}}\Delta M$, $\Delta\delta_{\mathrm{N}}\Delta M$, $\delta_{\mathrm{T}}\Delta\mu$, $\Delta\delta_{\mathrm{T}}\Delta\mu$ under some assumptions that involve:

- Perturbations in P- and S-wave moduli ΔM and $\Delta\mu$ are small;
- P-wave attenuation and its perturbation are weak (i.e. $\frac{1}{Q_{\mathrm{P}}} \ll 1$ and $\Delta\frac{1}{Q_{\mathrm{P}}} \ll 1$);
- Both normal and tangential layer-weaknesses and their perturbations are not too large (i.e. $\delta_{\mathrm{N}} < 1$, $\delta_{\mathrm{T}} < 1$, $\Delta\delta_{\mathrm{N}} < 1$, and $\Delta\delta_{\mathrm{T}} < 1$).

A relationship between P-to-P reflection coefficient R_{PP} and perturbation in stiffness matrix $\Delta\mathbf{C}$ is given by (Shaw and Sen, 2004, 2006; Moradi and Innanen, 2017; Chen and Innanen, 2018)

$$R_{\mathrm{PP}} = \frac{1}{4\rho\cos^2\theta}\left[\Delta\rho\cos 2\theta + \chi_{11}\Delta C_{11} + 2\chi_{13}\Delta C_{13} + \chi_{33}\Delta C_{33} + \chi_{55}\Delta C_{55}\right], \tag{8}$$

where θ is the incidence angle of P-wave, and the elements of χ are given by

$$\begin{aligned}
\chi_{11} &= \frac{\rho\sin^4\theta}{M}, \\
\chi_{13} &= \frac{\rho\sin^2\theta\cos^2\theta}{M}, \\
\chi_{33} &= \frac{\rho\cos^4\theta}{M}, \\
\chi_{55} &= \frac{-4\rho\sin^2\theta\cos^2\theta}{M}.
\end{aligned} \tag{9}$$

Substituting equations 7 and 9 into equation 8, we obtain a linearized and frequency-dependent P-to-P reflection coefficient after some algebra

$$\begin{aligned}
R_{\mathrm{PP}}(\theta, f) =& \frac{1}{4}\sec^2\theta\frac{\Delta M}{M} - 2\kappa\sin^2\theta\frac{\Delta\mu}{\mu} + \frac{\cos 2\theta}{4\cos^2\theta}\frac{\Delta\rho}{\rho} \\
&+ \left[\frac{1}{2}\sec^2\theta - 2\kappa\sin^2\theta\,(\xi+1)\right]\Gamma_f\Delta\frac{1}{Q_{\mathrm{P}}} \\
&- \frac{1}{4}\sec^2\theta\left(1 - 2\kappa\sin^2\theta\right)\Delta\delta_{\mathrm{N}} + \kappa\sin^2\theta\Delta\delta_{\mathrm{T}}.
\end{aligned} \tag{10}$$

Based on the P-to-P reflection coefficient, we next derive the corresponding anelastic impedance ($\mathcal{A}_{\mathrm{EI}}$) using approximations that involve

$$\frac{\Delta x}{x} \approx d\ln x,\ R_{\mathrm{PP}} \approx \frac{1}{2} d\ln\mathcal{A}_{\mathrm{EI}},\ \Delta x \approx dx, \tag{11}$$

where x refers to M, μ, ρ, $\frac{1}{Q_{\mathrm{P}}}$, δ_{N} and δ_{T}, respectively. Combining equations 10 and 11, we obtain the expression of anelastic impedance as

$$\mathcal{A}_{\mathrm{EI}}(\theta, f) = M^{\mathcal{P}_M(\theta)} \mu^{\mathcal{P}_\mu(\theta)} \rho^{\mathcal{P}_\rho(\theta)} \exp\left[\mathcal{P}_Q(\theta, f)\frac{1}{Q_{\mathrm{P}}} + \mathcal{P}_{\delta_{\mathrm{N}}}(\theta)\delta_{\mathrm{N}} + \mathcal{P}_{\delta_{\mathrm{T}}}(\theta)\delta_{\mathrm{T}}\right], \quad (12)$$

where

$$\begin{aligned}
\mathcal{P}_M(\theta) &= \frac{1}{2}\sec^2\theta, \\
\mathcal{P}_\mu(\theta) &= -4\kappa\sin^2\theta, \\
\mathcal{P}_\rho(\theta) &= \frac{\cos 2\theta}{2\cos^2\theta}, \\
\mathcal{P}_Q(\theta, f) &= \left[\sec^2\theta - 4\kappa\sin^2\theta(\xi+1)\right]\Gamma_f, \\
\mathcal{P}_{\delta_{\mathrm{N}}}(\theta) &= -\frac{1}{2}\sec^2\theta\left(1 - 2\kappa\sin^2\theta\right), \\
\mathcal{P}_{\delta_{\mathrm{T}}}(\theta) &= 2\kappa\sin^2\theta.
\end{aligned} \quad (13)$$

So far we have derived expressions of P-to-P linearized reflection coefficient and anelastic impedance, which will be the basis for estimating results of anelastic impedance from observed seismic data and predicting elastic parameters (M, μ and ρ), attenuation factor ($\frac{1}{Q_{\mathrm{P}}}$) and normal and tangential layer-weaknesses (δ_{N} and δ_{T}).

Following Whitcombe (2002), we propose the normalized anelastic impedance as

$$\begin{aligned}
\mathcal{A}_{\mathrm{EI}}(\theta, f) = &\left(\sqrt{M_0\rho_0}\right)\left(\frac{M}{M_0}\right)^{\mathcal{P}_M(\theta)}\left(\frac{\mu}{\mu_0}\right)^{\mathcal{P}_\mu(\theta)}\left(\frac{\rho}{\rho_0}\right)^{\mathcal{P}_\rho(\theta)} \\
&\exp\left[\mathcal{P}_Q(\theta, f)\frac{1}{Q_{\mathrm{P}}} + \mathcal{P}_{\delta_{\mathrm{N}}}(\theta)\delta_{\mathrm{N}} + \mathcal{P}_{\delta_{\mathrm{T}}}(\theta)\delta_{\mathrm{T}}\right],
\end{aligned} \quad (14)$$

where M_0, μ_0, and ρ_0 are constants of P- and S-wave moduli and density, which can provided by well log data.

Inversion of seismic amplitude data for elastic parameters, attenuation factor and layer-weaknesses

Prior to the prediction of unknown parameters that involve elastic parameters, attenuation factor and layer-weaknesses, we first implement the estimation of anelastic impedance datasets using partially-incidence-angle-stacked seismic data of two different dominant frequencies, which means we need to produce results of $\mathcal{A}_{\mathrm{EI}}(\theta_i, f_j)|_{i=1:6, j=1:2}$, which are preserved as the input data for estimating unknown parameters. The estimation of anelastic impedances is implemented using a model-based damped least-squares algorithm, which has well studied in our previous research (Chen et al., 2018a,c; Chen and Innanen, 2018).

In the present study, we focus on the establishment of an approach that utilizes estimated results of $\mathcal{A}_{\mathrm{EI}}$ to predict unknown parameters stably. In the case of l layer, a succinct

nonlinear relationship between the anelastic impedance vector $\mathbf{d}$ and the unknown parameter vector $\mathbf{m}$ is expressed as

$$\mathbf{d} = \mathbf{G}\left(\mathbf{m}\right), \tag{15}$$

where $\mathbf{G}$ is a nonlinear operator related to the incidence angle θ and frequency f, and

$$\begin{aligned} \mathbf{d} &= \mathbf{A}_{\mathrm{EI}}\left(\theta_i, f_j\right) = \begin{bmatrix} \mathcal{A}^1_{\mathrm{EI}}\left(\theta_i, f_j\right) \\ \vdots \\ \mathcal{A}^l_{\mathrm{EI}}\left(\theta_i, f_j\right) \end{bmatrix}, \\ \mathbf{m} &= \begin{bmatrix} \mathbf{M} \\ \boldsymbol{\mu} \\ \boldsymbol{\rho} \\ \mathbf{Q}_{\mathrm{n}} \\ \boldsymbol{\delta}_{\mathrm{N}} \\ \boldsymbol{\delta}_{\mathrm{T}} \end{bmatrix}, \end{aligned} \tag{16}$$

in which

$$\begin{aligned} \mathbf{M} = \begin{bmatrix} M_1 \\ \vdots \\ M_l \end{bmatrix}, \boldsymbol{\mu} = \begin{bmatrix} \mu_1 \\ \vdots \\ \mu_l \end{bmatrix}, \boldsymbol{\rho} = \begin{bmatrix} \rho_1 \\ \vdots \\ \rho_l \end{bmatrix}, \\ \mathbf{Q}_{\mathrm{n}} = \begin{bmatrix} 1/Q_1 \\ \vdots \\ 1/Q_l \end{bmatrix}, \boldsymbol{\delta}_{\mathrm{N}} = \begin{bmatrix} \left(\delta_{\mathrm{N}}\right)_1 \\ \vdots \\ \left(\delta_{\mathrm{N}}\right)_l \end{bmatrix}, \boldsymbol{\delta}_{\mathrm{T}} = \begin{bmatrix} \left(\delta_{\mathrm{T}}\right)_1 \\ \vdots \\ \left(\delta_{\mathrm{T}}\right)_l \end{bmatrix}, \end{aligned} \tag{17}$$

where subscripts $1, ..., l$ indicate the different layers.

Given an initial guess of unknown parameter vector $\mathbf{m}_0$ and values of incidence angle and frequency, we may compute the anelastic impedance using the derived equation 14. The L2-norm of data residual is expressed as

$$J = \frac{1}{2}\left[\mathbf{d} - \mathbf{G}\left(\mathbf{m}\right)\right]^T\left[\mathbf{d} - \mathbf{G}\left(\mathbf{m}\right)\right], \tag{18}$$

where J is to be minimized for obtaining acceptable inversion results of unknown parameter vector m. Based on the initial guess $\mathbf{m}_0$, the solution of unknown parameter vector is given by (Malinverno, 2002; Fukuda and Johnson, 2010; Köhn, 2011; Pan et al., 2016)

$$\mathbf{m} = \mathbf{m}_0 + \mathcal{L}\Delta\mathbf{m}, \tag{19}$$

where $\mathcal{L}$ is the step length, and $\Delta\mathbf{m}$ is the search direction. The full-Newton search direction $\Delta\mathbf{m}$ is given by

$$\Delta\mathbf{m} = -\mathbf{H}^{-1}\mathbf{g}, \tag{20}$$

where

$$\mathbf{g} = \begin{bmatrix} \frac{\partial \mathcal{A}_{\mathrm{EI}}}{\partial \mathbf{M}} \\ \frac{\partial \mathcal{A}_{\mathrm{EI}}}{\partial \boldsymbol{\mu}} \\ \frac{\partial \mathcal{A}_{\mathrm{EI}}}{\partial \boldsymbol{\rho}} \\ \frac{\partial \mathcal{A}_{\mathrm{EI}}}{\partial \mathbf{Q}_{\mathrm{n}}} \\ \frac{\partial \mathcal{A}_{\mathrm{EI}}}{\partial \boldsymbol{\delta}_{\mathrm{N}}} \\ \frac{\partial \mathcal{A}_{\mathrm{EI}}}{\partial \boldsymbol{\delta}_{\mathrm{T}}} \end{bmatrix} \begin{bmatrix} \Delta \mathbf{A}_{\mathrm{EI}} \\ \Delta \mathbf{A}_{\mathrm{EI}} \\ \Delta \mathbf{A}_{\mathrm{EI}} \\ \Delta \mathbf{A}_{\mathrm{EI}} \\ \Delta \mathbf{A}_{\mathrm{EI}} \\ \Delta \mathbf{A}_{\mathrm{EI}} \end{bmatrix},$$

$$\mathbf{H} \approx \begin{bmatrix} \frac{\partial^2 \mathcal{A}_{\mathrm{EI}}}{\partial \mathbf{M}^2} & & & & & & \\ & \frac{\partial^2 \mathcal{A}_{\mathrm{EI}}}{\partial \boldsymbol{\mu}^2} & & & & & \\ & & \frac{\partial^2 \mathcal{A}_{\mathrm{EI}}}{\partial \boldsymbol{\rho}^2} & & & & \\ & & & \frac{\partial^2 \mathcal{A}_{\mathrm{EI}}}{\partial \mathbf{Q}_{\mathrm{n}}{}^2} & & & \\ & & & & \frac{\partial^2 \mathcal{A}_{\mathrm{EI}}}{\partial \boldsymbol{\delta}_{\mathrm{N}}{}^2} & & \\ & & & & & \frac{\partial^2 \mathcal{A}_{\mathrm{EI}}}{\partial \boldsymbol{\delta}_{\mathrm{T}}{}^2} & \end{bmatrix} \begin{bmatrix} \Delta \mathbf{A}_{\mathrm{EI}} \\ \Delta \mathbf{A}_{\mathrm{EI}} \\ \Delta \mathbf{A}_{\mathrm{EI}} \\ \Delta \mathbf{A}_{\mathrm{EI}} \\ \Delta \mathbf{A}_{\mathrm{EI}} \\ \Delta \mathbf{A}_{\mathrm{EI}} \end{bmatrix} + \begin{bmatrix} \left(\frac{\partial \mathcal{A}_{\mathrm{EI}}}{\partial \mathbf{M}}\right)^2 & & & & & & \\ & \left(\frac{\partial \mathcal{A}_{\mathrm{EI}}}{\partial \boldsymbol{\mu}}\right)^2 & & & & & \\ & & \left(\frac{\partial \mathcal{A}_{\mathrm{EI}}}{\partial \boldsymbol{\rho}}\right)^2 & & & & \\ & & & \left(\frac{\partial \mathcal{A}_{\mathrm{EI}}}{\partial \mathbf{Q}_{\mathrm{n}}}\right)^2 & & & \\ & & & & \left(\frac{\partial \mathcal{A}_{\mathrm{EI}}}{\partial \boldsymbol{\delta}_{\mathrm{N}}}\right)^2 & & \\ & & & & & \left(\frac{\partial \mathcal{A}_{\mathrm{EI}}}{\partial \boldsymbol{\delta}_{\mathrm{T}}}\right)^2 & \end{bmatrix}, \tag{21}$$

in which $\Delta \mathcal{A}_{\mathrm{EI}}$ is the difference between the input anelastic impedance and that generated using the initial guess $\mathbf{m}_0$. We stress that both the gradient $\mathbf{g}$ and the Hessian matrix $\mathbf{H}$ are obtained via computing the derivative of anelastic impedance with respect to $\mathbf{m}$ using equation 14.

We next employ the Bayesian Markov chain Monte Carlo (MCMC) algorithm to implement the generation of candidates that are acceptable for computing the final inversion results of unknown parameters. One advantage of the MCMC algorithm is that the candidate of $\mathbf{m}$, $\mathbf{m}_{i+1}^{'}$, is generated by perturbing the current state $\mathbf{m}_i^{'}$ (for the first iteration $\mathbf{m}_1^{'} = \mathbf{m}_0$) following a Markov chain random walk. In the present study, we let the step length $\mathcal{L}$ be a [-1, 1] uniform random number, and using equation 18 we generate the candidate combining the initial guess and the full-Newton step. In the Bayesian framework, we determine whether the generated candidate should be accepted or not using a probability estimation

$$P_{\mathrm{c}}\left(\mathbf{m}_{i+1}^{'}\right) = \min\left[1, \frac{P\left(\mathbf{m}_{i+1}^{'}|\mathbf{d}\right)}{P\left(\mathbf{m}_{i}^{'}|\mathbf{d}\right)}\right], \tag{22}$$

where $P\left(\mathbf{m}_{i+1}^{'}|\mathbf{d}\right)$ and $P\left(\mathbf{m}_{i}^{'}|\mathbf{d}\right)$ are posterior probabilities that are computed based on the Bayesian theorem (Appendix A). Table 1 shows the scheme of the inversion method.

Table 1. The scheme of the inversion method

1. Construct initial guess $\mathbf{m}_0$ and let $\mathbf{m}_1 = \mathbf{m}_1^{'} = \mathbf{m}_0$;

2. **for** $j = 1, 2, ..., 20$

3. Compute $\Delta\mathbf{m}_j = -\mathbf{H}^{-1}\mathbf{g}$ using $\mathbf{m}_j$;

4. **for** $i = 1, 2, ..., 100$

5. Step1: Generate $\mathbf{m}_{i+1}^{'} = \mathbf{m}_i^{'} + \mathcal{L}\Delta\mathbf{m}_j,\ \mathcal{L} \in [-1, 1]$;

6. Step2: Estimate $P_{\mathrm{c}}\left(\mathbf{m}_{i+1}^{'}\right)$;

7. Step3: Determine if $\mathbf{m}_{i+1}^{'}$ is acceptable;
Yes, save $\mathbf{m}_{i+1}^{'}$;
No, go back to Step1;

8. **end**

9. Calculate the average values of all the accepted candidates, $\mathbf{m}_{\mathrm{a}}^{'}$, and let $\mathbf{m}_{j+1} = \mathbf{m}_{\mathrm{a}}^{'}$;

10. **end**

11. Compute the average value, $\mathbf{m}_{\mathrm{a}} = \frac{1}{20}\Sigma_{j=1}^{j=20}\mathbf{m}_j$, and preserve $\mathbf{m}_{\mathrm{a}}$ as the final inversion result.

We next explain how to determine whether the generated candidate is acceptable or not. The determination is implemented as:

- Given a generated candidate $\mathbf{m}^{'}$, we compute the acceptance probability $P_{\mathrm{c}}\left(\mathbf{m}^{'}\right)$ using equation 21;
- Generate a random value β, and $\beta \in [0, 1]$;
- Compare β with $P_{\mathrm{c}}\left(\mathbf{m}^{'}\right)$; if $\beta < P_{\mathrm{c}}\left(\mathbf{m}^{'}\right)$, accept the generated candidate, otherwise generate a new candidate again.

We stress that in the proposed inversion approach there are two loops: the inner loop is implemented based on the Bayesian MCMC inversion algorithm to generate acceptable candidates using the Newton-step $\Delta\mathbf{m}$ computed in the outer loop; and the acceptable candidates generated in the inner loop will again provide the model vector that is the average value of all the acceptable candidates to compute the Newton-step again in the outer loop.

NUMERICAL EXAMPLES

Verifying the accuracy of derived reflection coefficient

A two-layer model

In order to verify the accuracy of derived reflection coefficient, we first utilize a two-layer model to compare PP-wave reflection coefficients computed using the derived equation 10, approximate results calculated using the linearized reflection coefficient proposed by Behura and Tsvankin (2009) for arbitrarily anisotropic media (Appendix B), and exact solutions obtained using the generalized Zoeppritz equations (Schoenberg and Protazio, 1990; Chen et al., 2018d), as shown in Figure 3. Table 2 shows elastic parameters, inverse P-wave quality factors and layer-weaknesses of two-layer model.

Table 2. Parameters of two-layer model

	$M\,(\mathrm{GPa})$	$\mu\,(\mathrm{GPa})$	$\rho\,(\mathrm{g/cm^3})$	$1/Q_{\mathrm{P}}\,(-)$	$\delta_{\mathrm{N}}\,(-)$	$\delta_{\mathrm{T}}\,(-)$
Layer1	20.70	8.30	2.30	0.10	0.06	0.02
Layer2	12.50	3.38	2.00	0.50	0.34	0.11

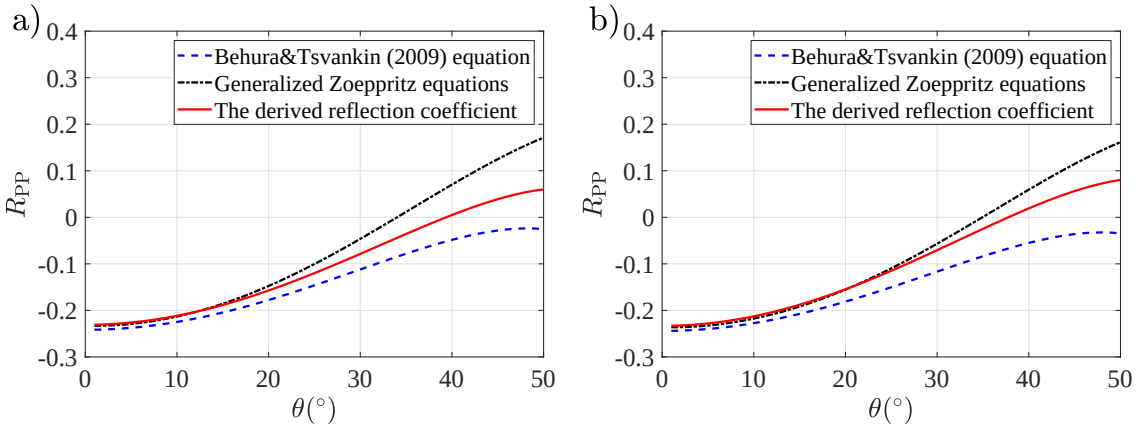

FIG. 3. Comparisons between PP-wave reflection coefficients computed using the derived linearized equation, approximate equation proposed by Behura and Tsvankin (2009), and generalized Zoeppritz equations. a) $f = 10\mathrm{Hz}$, and b) $f = 30\mathrm{Hz}$. The reference frequency f_{r} used in the calculation is $3000\mathrm{Hz}$.

In Figure 3 we observe that differences between PP-wave reflection coefficients computed using the derived equation 10 and exact solutions calculated using the generalized Zoeppritz equations are relatively small in the case of the maximum incidence angle being around 30°, which confirms the derived equation is acceptable for computing PP-wave reflection coefficient in the case of the incidence angle θ being less than 30°. We also observe that the derived reflection coefficient has a relatively high accuracy than the approximate reflection coefficient proposed by Behura and Tsvankin (2009).

A well-log model

We next use a well-log model to further verify the accuracy of the derived linearized reflection coefficient. Figure 4(a) plots curves of P- and S-wave moduli and density, and Figure 4(b) plots constructed curves of P-wave inverse quality factor and layer-weaknesses. The curve of P-wave attenuation factor $\frac{1}{Q_{\mathrm{P}}}$ is constructed using the $fakeq$ function proposed by Margrave (2013). Following Li (2006), we first compute Thomsen anisotropic parameters using empirical relationships, and then we roughly calculate layer-weaknesses according to definitions of Thomsen anisotropic parameters and their approximations (Appendix C). In Figure 4 we observe around the location of reservoir (1180ms) P- and S-wave moduli and density exhibit relatively low values and the constructed P-wave attenuation factor and layer-weaknesses show relatively high values.

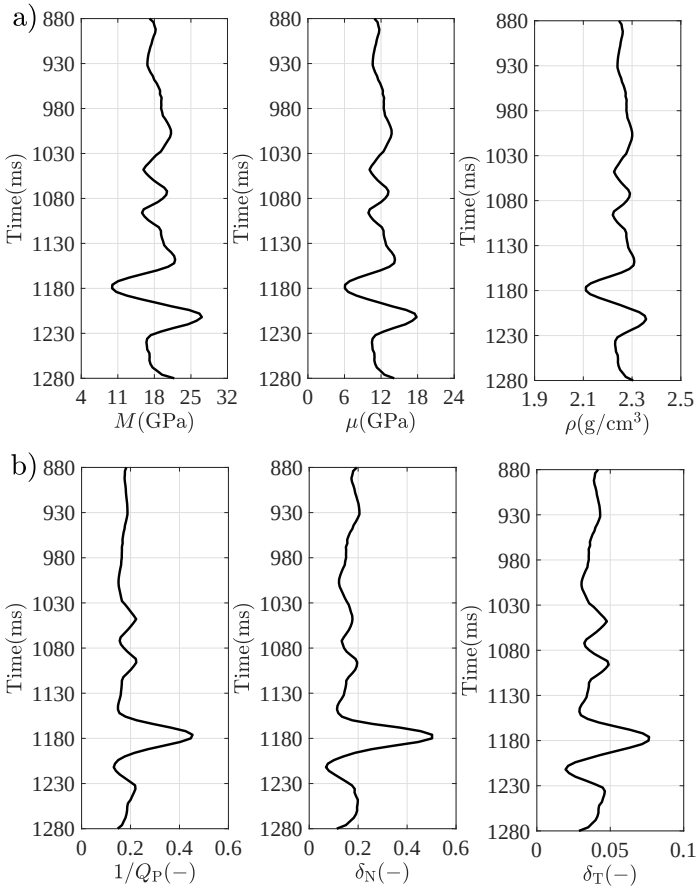

FIG. 4. Curves of well log model.

We compute PP-wave reflection coefficients using the derived equation 10 and the generalized Zoeppritz equations in the case of different frequencies ($f_1 = 8$Hz and $f_2 = 30$Hz), and utilizing Ricker wavelets of dominant frequencies 8Hz and 20Hz, we generate synthetic seismic data using the computed results of PP-wave reflection coefficients in the case of incidence angle being $1^\circ - 50^\circ$. Comparisons between the generated synthetic seismic data are plotted in Figure 5.

In Figure 5 we observe there is a good match between the synthetic seismic data re-

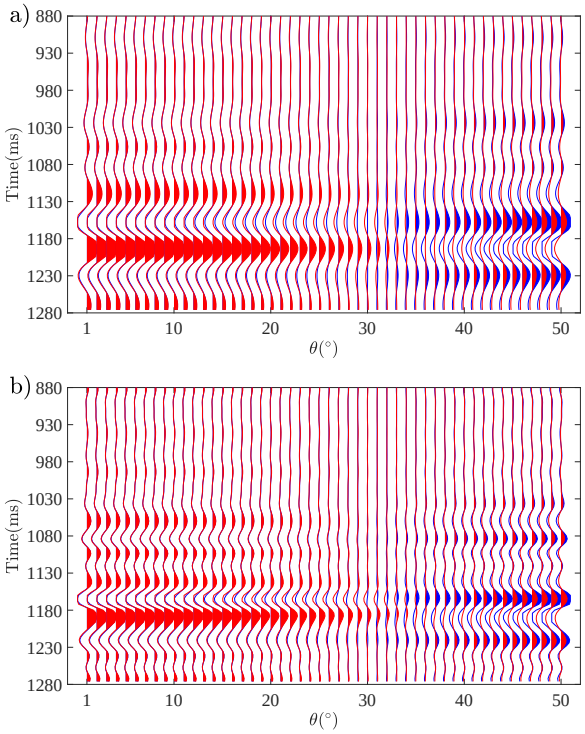

FIG. 5. Comparisons between synthetic seismic data generated using PP-wave reflection coefficients computed using the derived linearized equation (red color) and the Zoeppritz equations (blue color). a) $f = 8\text{Hz}$, and b) $f = 30\text{Hz}$. The reference frequency f_{r} used in the calculation is 3000Hz.

spectively generated using PP-wave reflection coefficients computed utilizing the derived linearized equation and Zoeppritz equations, which confirms that the derived equation can produce PP-wave reflection coefficients of high accuracy in the case that the incidence angle is less than 30° (i.e. $\theta \leq 30^\circ$).

Verifying robustness and stability of the proposed inversion approach

Again using the well-log model, we first generate synthetic seismic data in the case of the incidence angle being $1^\circ - 30^\circ$ utilizing the generalized Zoeppritz equations, and then we add Gaussian random noise into the synthetic data, from which we obtain the seismic data of signal-to-noise ratio (SNR) of 2. The noisy seismic data are preserved as the input for estimating anelastic impedances. Figure 6 plots seismic data of SNR of 2, which are generated using PP-wave reflection coefficients computed at frequencies $f_1 = 8\text{Hz}$ and $f_2 = 30\text{Hz}$, and Ricker wavelets of dominant frequencies f_1 and f_2.

Using the noisy synthetic seismic data we first generate six partially incidence-angle-stacked seismic data, which are obtained by stacking synthetic seismic data over different ranges of incidence angle, i.e., $1^\circ - 5^\circ$, $6^\circ - 10^\circ$, $11^\circ - 15^\circ$, $16^\circ - 20^\circ$, $21^\circ - 25^\circ$ and $26^\circ - 30^\circ$. We let the central angles be $\theta_1 = 3^\circ$, $\theta_2 = 8^\circ$, $\theta_3 = 13^\circ$, $\theta_4 = 18^\circ$, $\theta_5 = 23^\circ$, and $\theta_6 = 28^\circ$. With the stacked seismic data in hand, we implement the inversion for anelastic imepdances using the model-constrained damping least-squares algorithm proposed by Chen et al. (2018a). Comparisons between inversion results of anelastic impedance and true values computed using equation 14 are plotted in Figure 7.

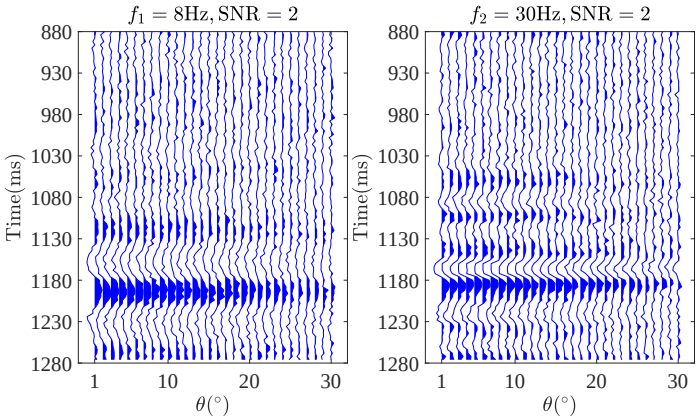

FIG. 6. Synthetic seismic data of signal-to-noise ratio (SNR) of 2. The reference frequency f_r used in the calculation is 3000Hz.

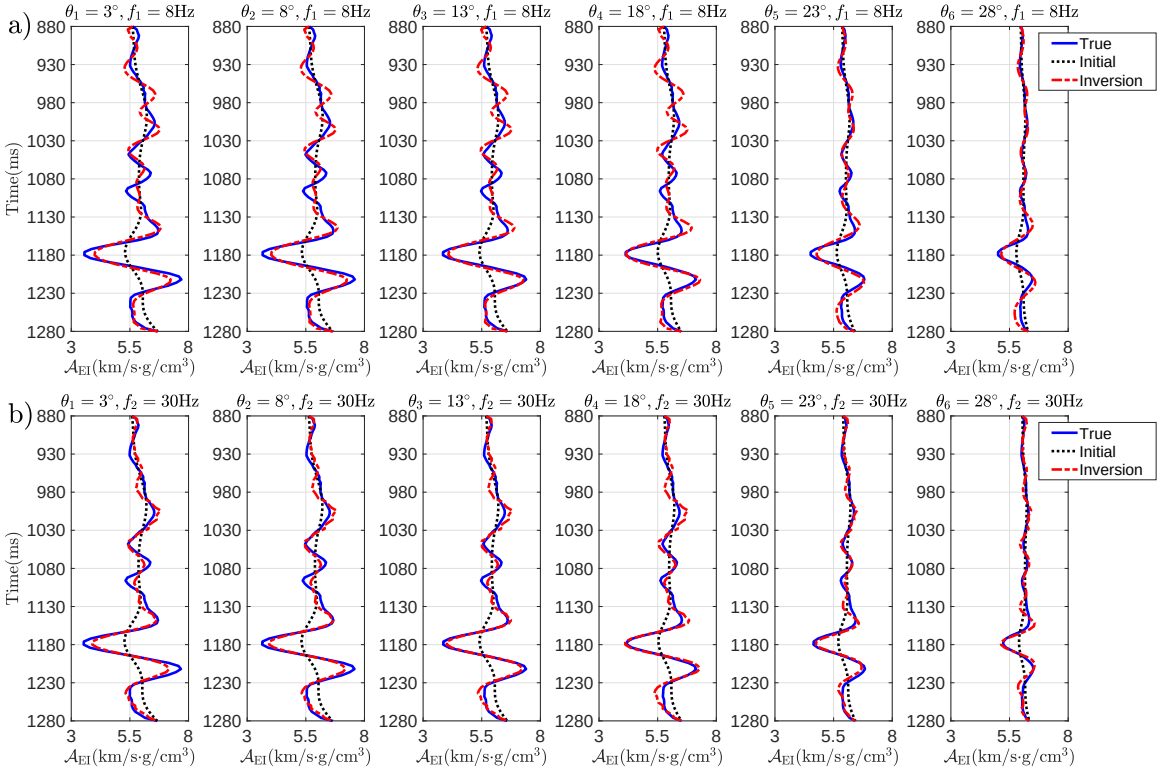

FIG. 7. Comparisons between inversion results and true values of anelastic impedances. a) $f_1 = 8\text{Hz}$, and b) $f_2 = 30\text{Hz}$. The dotted curve indicates the initial model, which is a smoothed version of true value.

In Figure 7 we observe that the anelastic impedance around the location of gas reservoir (1180ms) exhibit a relatively low value, and the inversion results of anelastic impedance obtained from the partially incidence-angle-stacked seismic data can match the true values computed using the derived expression of anelastic impedance well even in the case of SNR being 2, which confirms that the inverted anelastic impedances can be used for the estimation of unknown parameters that involve P- and S-wave moduli, density, P-wave attenuation factor and layer-weaknesses.

With the inversion results of anelastic impedance in hand, we proceed to the estimation

of unknown parameters using the proposed nonlinear inversion approach and workflow outlined in the previous section. Figure 8 plots comparisons between the acceptable inversion results and true values, in which the final inversion results computed using all the acceptable results are plotted.

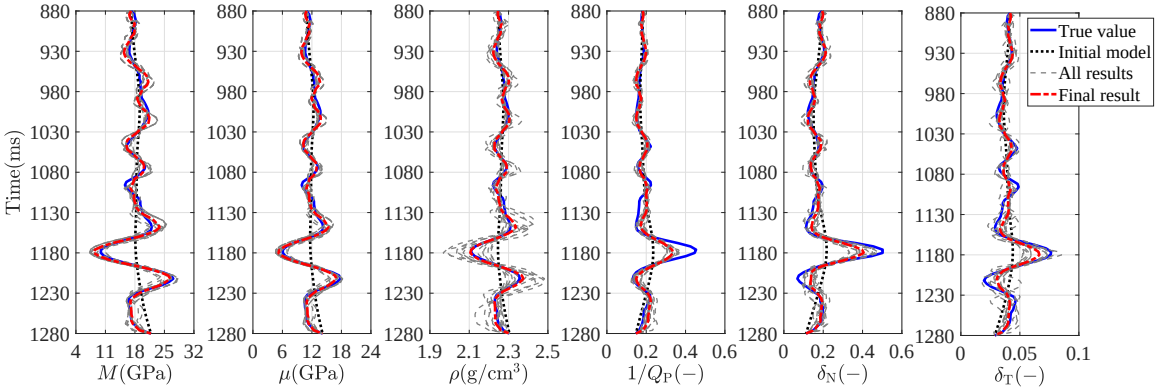

FIG. 8. Comparisons between all the inversion results and true values of unknown parameters.

In Figure 8 we observe that there is a good match between the inversion result and the true value, which confirms that the proposed nonlinear inversion method that combines the full-Newton step and Bayesian MCMC inversion can produce reliable results of P- and S-wave moduli, density, attenuation factors and layer-weaknesses even the case of SNR of 2, and also reveals that the proposed inversion method is stable and robust.

Field data example

We proceed to employing a field data set to further verify the proposed inversion approach and workflow. The seismic data, which are provided as common-imaging-point (CIP) gathers, were acquired above a shale gas reservoir located in China. Using well log data we first transfer the CIP gathers to angle gathers in a commercial software package. Figure 9 plots the profile of angle gathers extracted at the location of a successfully drilling well.

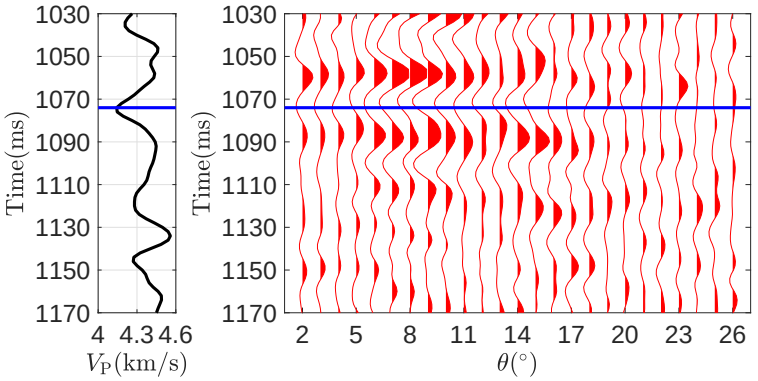

FIG. 9. Angle gathers extracted at the location of well log. The blue line indicates the location of gas reservoir.

Comparing P-wave velocity and the angle gathers, we observe around the location of gas reservoir the P-wave velocity exhibits a relatively low value and there is a feature that

the seismic amplitudes vary with the incidence angle (AVA). We next produce partially incidence-angle-stacked seismic data using the angle gathers, and then we extract frequency components from the stacked seismic data. Seismic data of different angle ranges ($2^\circ - 6^\circ$, $6^\circ - 10^\circ$, $10^\circ - 14^\circ$, $14^\circ - 18^\circ$, $18^\circ - 22^\circ$, and $22^\circ - 26^\circ$) are utilized to generate partially-incidence-angle stacked seismic data, and we assume the central incidence angles of stacked seismic data are $\theta_1 = 4^\circ$, $\theta_2 = 8^\circ$, $\theta_3 = 12^\circ$, $\theta_4 = 16^\circ$, $\theta_5 = 20^\circ$, and $\theta_6 = 24^\circ$. Two rectangle filters are respectively employed to extract the frequency components of 3Hz-13Hz and 25-35Hz, and we assume the central frequencies of the extracted components are $f_1 = 8$Hz and $f_2 = 30$Hz. Figure 10 plots the partially incidence-angle-stacked seismic data of different central incidence angles and frequencies.

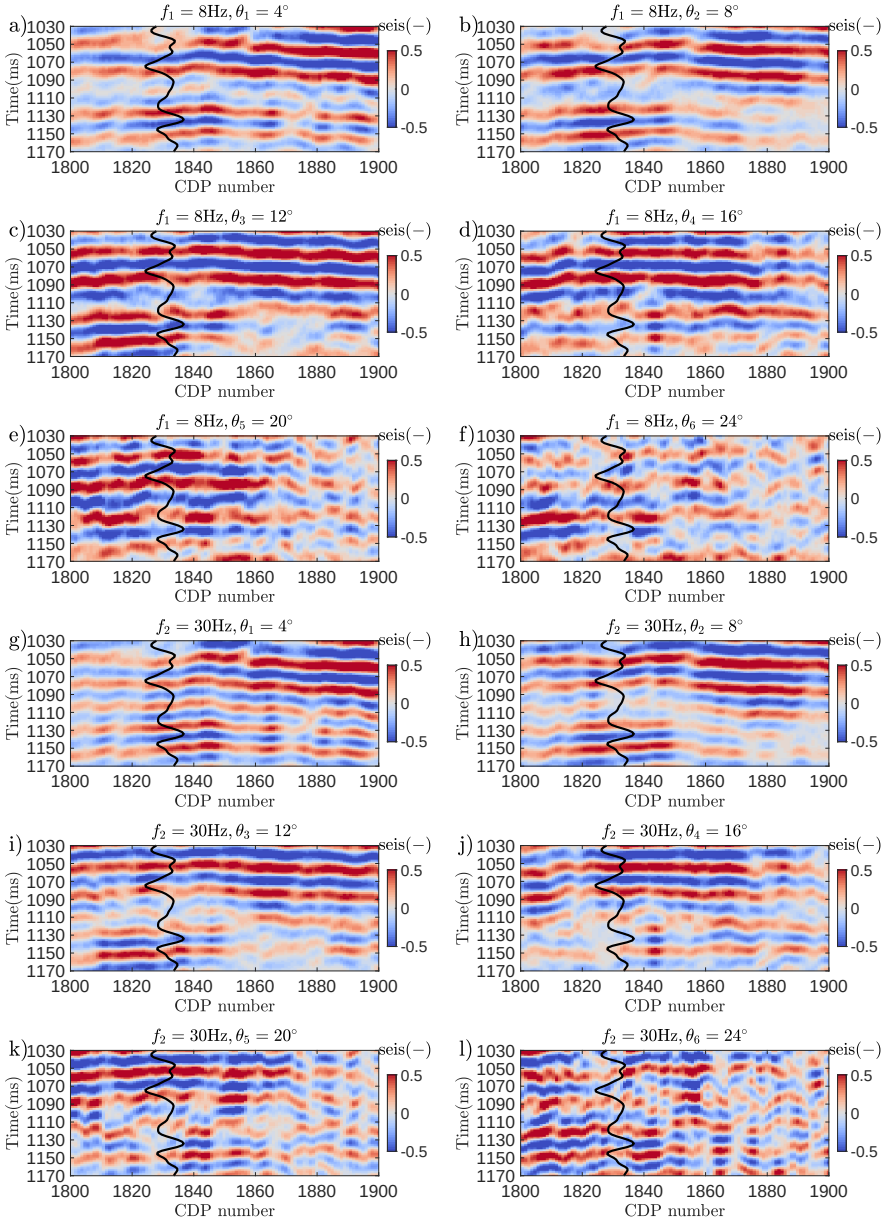

FIG. 10. Profiles of seismic data. The black curve in the figure indicates P-wave velocity.

Using the extracted frequency components of partially incidence-angle-stacked seismic

data we first implement the inversion for anelastic impedances using the least-squares algorithm proposed by Chen et al. (2018a). Figure 11 plots inversion results of anelastic impedance.

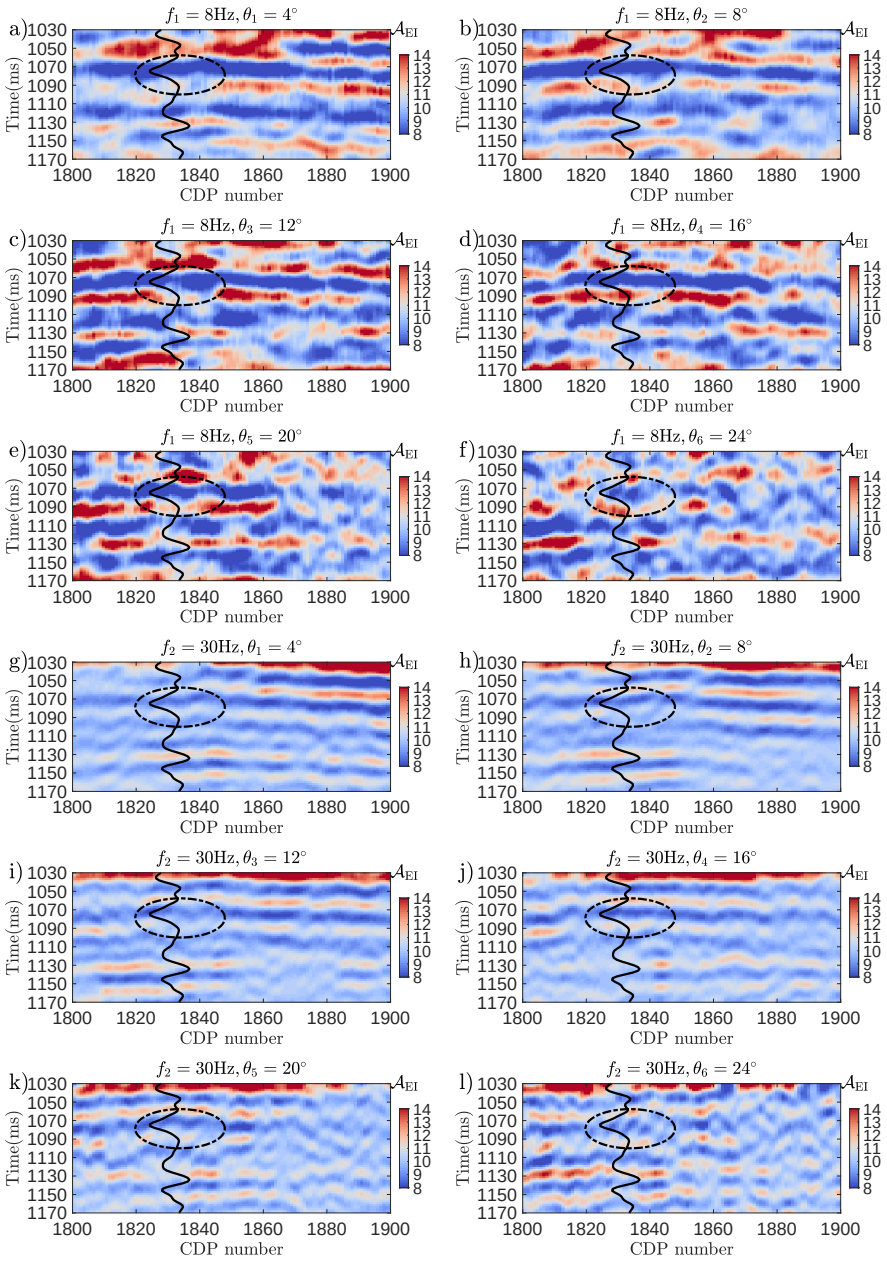

FIG. 11. Inversion results of anelastic impedance of different incidence angles and frequencies. The black curve in the figure indicates P-wave velocity, and the dashed ellipse indicates the location of gas reservoir.

In Figure 11 we observe that around the location of gas reservoir the inverted anelastic impedance exhibits a relatively low value, which is in agreement with the feature we observed in anelastic impedances computed using the well log model in the previous section. Prior to implementing the nonlinear inversion for P- and S-wave moduli, density, P-wave attenuation factor and layer-weaknesses, we first construct initial models of unknown parameters. We implement AVA inversion for P- and S-wave velocities and density using

a commercial software package, and then we roughly calculate P- and S-wave moduli. The method to construct initial models of P-wave attenuation factor and layer-weaknesses is discussed in the previous section, in which the $fakeq$ function and the empirical relationships (Appendix C) are employed. Smoothed version of the roughly estimated P- and S-wave moduli, density, attenuation factor and layer-weaknesses are used as initial models in the nonlinear inversion, as plotted in Figure 12.

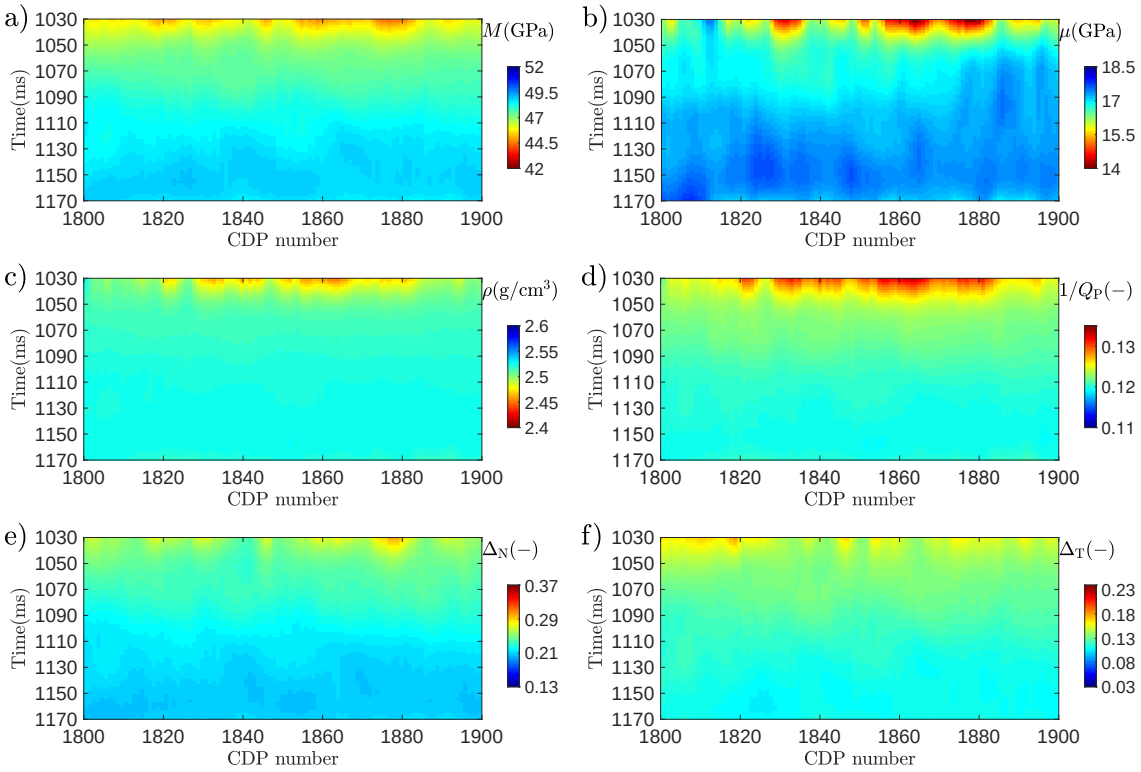

FIG. 12. Constructed initial models of P- and S-wave moduli, density, P-wave attenuation factor and layer-weaknesses.

Using the proposed nonlinear inversion approach and workflow, we implement the prediction of P- and S-wave moduli, density, P-wave attenuation factor and layer-weaknesses using the estimated anelastic impedances. Figure 13 plots the inversion results of unknown parameters, and we observe that around the location of gas-reservoir the inverted P- and S-wave moduli and density exhibit relative low values, and the estimated P-wave attenuation factor and layer-weaknesses exhibit relatively high values. It indicates that seismic wave propagation in the shale gas reservoir exhibits both high attenuation and large anisotropy.

CONCLUSIONS

Beginning with the periodically layered model, we express simplified frequency-dependent stiffness parameters in terms of attenuation factor and layer-weaknesses. Using perturbations in stiffness parameters, which involves perturbations in attenuation factors and layer-weaknesses, we derive the frequency-dependent and linearized P-to-P reflection coefficient as a function of reflectivities of P- and S-wave moduli and density and changes in attenuation factor and lay-weaknesses across the reflection interface; and we also propose the expression of anisotropic anelastic impedance ($\mathcal{A}_{\rm EI}$). Based on the derived reflection co-

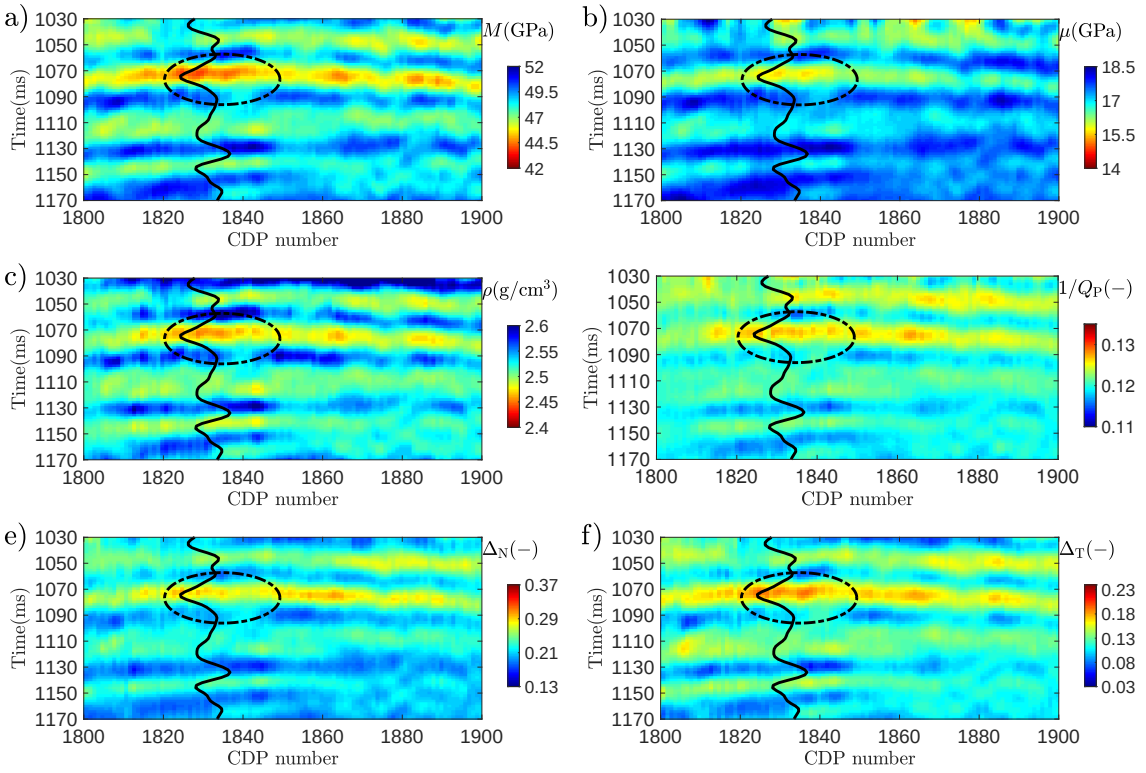

FIG. 13. Inversion results of P- and S-wave moduli, density, P-wave attenuation factor and layer-weaknesses. The black curve indicates the P-wave velocity, and the ellipse indicates the location of gas-reservoir.

efficient and anelastic impedance, we establish an inversion approach and workflow of employing different frequency components of partially-incidence-stacked seismic data to estimate the unknown parameter vector involving P- and S-wave moduli, density, attenuation factor and layer-weaknesses using a Bayesian Markov chain Monte Carlo algorithm. Test on synthetic data confirms that the inversion approach may produce stable results of unknown parameters in the case of signal-to-noise ratio (SNR) of 2. We finally apply the inversion approach and workflow to real data sets acquired over a shale reservoir, from which reliable results of attenuation factor and lay-weaknesses that well match the reservoir, are obtained. We conclude that the proposed inversion approach appears to be a useful tool for estimating attenuation and anisotropy for underground layers and reservoirs.

ACKNOWLEDGMENTS

We thank the sponsors of CREWES for continued support. This work was funded by CREWES industrial sponsors, and NSERC (Natural Science and Engineering Research Council of Canada) through the grant CRDPJ 461179-13. This work was also funded in part thanks to the Canada First Research Excellence Fund, and the Mitacs Accelerate grant *Responsible Development of Unconventional Hydrocarbon Reserves*. The SINOPEC Key Lab of Multi-Component Seismic Technology is thanked for providing the processed real data.

APPENDIX A. ESTIMATING PROBABILITY FOR DETERMINING AN ACCEPTABLE CANDIDATE

Following Chen et al. (2017), we express the posterior probability distribution function (PDF) $P(\mathbf{m}|\mathbf{d})$ as

$$P(\mathbf{m}|\mathbf{d}) = P(\mathbf{d}|\mathbf{m})\, P(\mathbf{m}), \tag{A.1}$$

where $P(\mathbf{d}|\mathbf{m})$ is the likelihood function, and $P(\mathbf{m})$ is the prior probability function. In the present study, we assume both the likelihood function and the prior probability are consistent with the Gaussian distribution; hence the posterior PDF is expressed as

$$P(\mathbf{m}|\mathbf{d}) \propto \exp\left\{\begin{array}{c} -\sum\frac{[\mathbf{d}-\mathbf{G}(\mathbf{m})]^T[\mathbf{d}-\mathbf{G}(\mathbf{m})]}{2\sigma_{\mathbf{e}}^2} \\ -\sum\frac{(\boldsymbol{M}-\psi_{\mathbf{M}})^T(\boldsymbol{M}-\psi_{\mathbf{M}})}{2\sigma_{\mathbf{M}}^2} - \sum\frac{(\boldsymbol{\mu}-\psi_{\boldsymbol{\mu}})^T(\boldsymbol{\mu}-\psi_{\boldsymbol{\mu}})}{2\sigma_{\boldsymbol{\mu}}^2} \\ -\sum\frac{(\boldsymbol{\rho}-\psi_{\boldsymbol{\rho}})^T(\boldsymbol{\rho}-\psi_{\boldsymbol{\rho}})}{2\sigma_{\boldsymbol{\rho}}^2} - \sum\frac{\left(\mathbf{Q}_{\mathrm{n}}-\psi_{\mathbf{Q}_{\mathrm{n}}}\right)^T\left(\mathbf{Q}_{\mathrm{n}}-\psi_{\mathbf{Q}_{\mathrm{n}}}\right)}{2\sigma_{\mathbf{Q}_{\mathrm{n}}}^2} \\ -\sum\frac{\left(\boldsymbol{\delta}_{\mathrm{N}}-\psi_{\boldsymbol{\delta}_{\mathrm{N}}}\right)^T\left(\boldsymbol{\delta}_{\mathrm{N}}-\psi_{\boldsymbol{\delta}_{\mathrm{N}}}\right)}{2\sigma_{\boldsymbol{\delta}_{\mathrm{N}}}^2} - \sum\frac{\left(\boldsymbol{\delta}_{\mathrm{T}}-\psi_{\boldsymbol{\delta}_{\mathrm{T}}}\right)^T\left(\boldsymbol{\delta}_{\mathrm{T}}-\psi_{\boldsymbol{\delta}_{\mathrm{T}}}\right)}{2\sigma_{\boldsymbol{\delta}_{\mathrm{T}}}^2} \end{array}\right\}, \tag{A.2}$$

where $\psi_{\mathbf{M}}$, $\psi_{\boldsymbol{\mu}}$, $\psi_{\boldsymbol{\rho}}$, $\psi_{\mathbf{Q}_{\mathrm{n}}}$, $\psi_{\boldsymbol{\delta}_{\mathrm{N}}}$, and $\psi_{\boldsymbol{\delta}_{\mathrm{T}}}$ respectively represent average values of corresponding vectors, $\sigma_{\mathbf{M}}^2$, $\sigma_{\boldsymbol{\mu}}^2$, $\sigma_{\boldsymbol{\rho}}^2$, $\sigma_{\mathbf{Q}_{\mathrm{n}}}^2$, $\sigma_{\boldsymbol{\delta}_{\mathrm{N}}}^2$, and $\sigma_{\boldsymbol{\delta}_{\mathrm{T}}}^2$ respectively variance values of corresponding vectors, and $\sigma_{\mathbf{e}}^2$ represents the variance of errors/noises between input data and modeled data.

APPENDIX B. PP-WAVE REFLECTION COEFFICIENT FOR ATTENUATIVE AND ARBITRARILY ANISOTROPIC MEDIA

In the case of attenuative and arbitrarily anisotropic media, Behura and Tsvankin (2009) proposed a linearized PP-wave reflection coefficient $R_{\mathrm{PP}}^{\mathrm{H}}$ as

$$\begin{aligned} R_{\mathrm{PP}}^{\mathrm{H}} =& \frac{\Delta\rho}{2\rho} + \frac{\Delta C_{33}}{4\rho V_{\mathrm{Pa}}^2} + \left(\frac{\Delta C_{13}}{2\rho V_{\mathrm{Pa}}^2} - \frac{\Delta C_{33}}{4\rho V_{\mathrm{Pa}}^2} - \frac{\Delta C_{55}}{\rho V_{\mathrm{Pa}}^2} - \frac{2V_{\mathrm{Sa}}^2}{V_{\mathrm{Pa}}^2}\frac{\Delta\rho}{\rho}\right)\sin^2\theta \\ &+ \frac{\Delta C_{11}}{4\rho V_{\mathrm{Pa}}^2}\sin^2\theta\tan^2\theta, \end{aligned} \tag{B.1}$$

where

$$\begin{aligned} V_{\mathrm{Pa}} =& \sqrt{\frac{\mathcal{M}}{\rho}}, \\ V_{\mathrm{Sa}} =& \sqrt{\frac{\mathcal{U}}{\rho}}. \end{aligned} \tag{B.2}$$

APPENDIX C. APPROXIMATE RELATIONSHIPS BETWEEN THOMSEN ANISOTROPIC PARAMETERS AND LAYER-WEAKNESSES

Based on the rock physic template and core data, Li (2006) proposed empirical relationships between Thomsen anisotropic parameters and clay volume

$$\begin{aligned}\varepsilon =&\frac{0.6V_{\rm clay}\left(V_{\rm P}-V_{\rm P}^{\rm water}\right)}{V_{\rm P}^{\rm quartz}-V_{\rm P}^{\rm water}-2.65V_{\rm clay}},\\ \gamma =&\frac{0.67V_{\rm clay}V_{\rm S}}{V_{\rm S}^{\rm quartz}-2.29V_{\rm clay}},\end{aligned} \tag{C.1}$$

where $V_{\rm clay}$ is the clay volume, $V_{\rm P}$ and $V_{\rm S}$ are P and S-wave velocities provided by well log, and in the present study, $V_{\rm P}^{\rm water}=1.5{\rm km/s}$, $V_{\rm P}^{\rm quartz}=6.05{\rm km/s}$, and $V_{\rm S}^{\rm quartz}=4.09{\rm km/s}$.

According to definitions of Thomsen anisotropic parameters (Thomsen, 1986), we obtain approximate relationships between Thomsen anisotropic parameters and layer-weaknesses as

$$\begin{aligned}\varepsilon =&\frac{C_{11}-C_{33}}{2C_{33}}\approx 2\kappa(1-\kappa)\delta_{\rm N},\\ \gamma =&\frac{C_{66}-C_{44}}{2C_{44}}\approx\frac{1}{2}\delta_{\rm T}.\end{aligned} \tag{C.2}$$

Combining equations C.1 and C.2 we may first compute Thomsen anisotropic parameters using clay volume, and then we roughly calculate layer-weaknesses using the computed anisotropic parameters.

REFERENCES

Aki, K., and Richards, P. G., 2002, Quantitative seismology: University science books.

Alkhalifah, T., and Tsvankin, I., 1995, Velocity analysis for transversely isotropic media: Geophysics, **60**, No. 5, 1550–1566.

Backus, G. E., 1962, Long-wave elastic anisotropy produced by horizontal layering: Journal of Geophysical Research, **67**, No. 11, 4427–4440.

Bakulin, A., Grechka, V., and Tsvankin, I., 2000, Estimation of fracture parameters from reflection seismic data—Part I: HTI model due to a single fracture set: Geophysics, **65**, No. 6, 1788–1802.

Behura, J., and Tsvankin, I., 2009, Reflection coefficients in attenuative anisotropic media: Geophysics, **74**, No. 5, WB193–WB202.

Bird, C., 2012, Amplitude-variation-with frequency (AVF) analysis of seismic data over anelastic targets: M.Sc. thesis, University of Calgary.

Borcherdt, R. D., 2009, Viscoelastic waves in layered media: Cambridge University Press.

Brajanovski, M., Gurevich, B., and Schoenberg, M., 2005, A model for P-wave attenuation and dispersion in a porous medium permeated by aligned fractures: Geophysical Journal International, **163**, No. 1, 372–384.

Carcione, J. M., 2015, Wave fields in real media: Wave propagation in anisotropic, anelastic, porous and electromagnetic media, vol. 38: Elsevier.

Chapman, M., 2003, Frequency-dependent anisotropy due to meso-scale fractures in the presence of equant porosity: Geophysical Prospecting, **51**, No. 5, 369–379.

Chen, H., and Innanen, K. A., 2018, Estimation of fracture weaknesses and integrated attenuation factors from azimuthal variations in seismic amplitudes: Geophysics, **83**, No. 6, R711–R723.

Chen, H., Innanen, K. A., and Chen, T., 2018a, Estimating P-and S-wave inverse quality factors from observed seismic data using an attenuative elastic impedance: Geophysics, **83**, No. 2, R173–R187.

Chen, H., Ji, Y., and Innanen, K. A., 2018b, Estimation of modified fluid factor and dry fracture weaknesses using azimuthal elastic impedance: Geophysics, **83**, No. 1, WA73–WA88.

Chen, H., Ji, Y., and Innanen, K. A., 2018c, Estimation of modified fluid factor and dry fracture weaknesses using azimuthal elastic impedance: Geophysics, **83**, No. 1, WA73–WA88.

Chen, H., Pan, X., Ji, Y., and Zhang, G., 2017, Bayesian Markov Chain Monte Carlo inversion for weak anisotropy parameters and fracture weaknesses using azimuthal elastic impedance: Geophysical Journal International, **210**, No. 2, 801–818.

Chen, H., Zhang, G., Chen, T., and Yin, X., 2018d, Joint PP-and PSV-wave amplitudes versus offset and azimuth inversion for fracture compliances in horizontal transversely isotropic media: Geophysical Prospecting, **66**, No. 3, 561–578.

Downton, J., and Roure, B., 2010, Azimuthal simultaneous elastic inversion for fracture detection, *in* SEG Technical Program Expanded Abstracts 2010, Society of Exploration Geophysicists, 263–267.

Downton, J. E., and Roure, B., 2015, Interpreting azimuthal Fourier coefficients for anisotropic and fracture parameters: Interpretation, **3**, No. 3, ST9–ST27.

Dvorkin, J. P., and Mavko, G., 2006, Modeling attenuation in reservoir and nonreservoir rock: The Leading Edge, **25**, No. 2, 194–197.

Fukuda, J., and Johnson, K. M., 2010, Mixed linear—non-linear inversion of crustal deformation data: Bayesian inference of model, weighting and regularization parameters: Geophysical Journal International, **181**, No. 3, 1441–1458.

Grechka, V., Tsvankin, I., Bakulin, A., Hansen, J. O., and Signer, C., 2002, Joint inversion of PP and PS reflection data for VTI media: A North Sea case study.

Guo, J., Germán Rubino, J., Barbosa, N. D., Glubokovskikh, S., and Gurevich, B., 2018, Seismic dispersion and attenuation in saturated porous rocks with aligned fractures of finite thickness: Theory and numerical simulations—part 1: P-wave perpendicular to the fracture plane: Geophysics, **83**, No. 1, WA49–WA62.

Gurevich, B., Brajanovski, M., Galvin, R. J., Müller, T. M., and Toms-Stewart, J., 2009, P-wave dispersion and attenuation in fractured and porous reservoirs–poroelasticity approach: Geophysical Prospecting, **57**, No. 2, 225–237.

Hsu, C.-J., and Schoenberg, M., 1993, Elastic waves through a simulated fractured medium: Geophysics, **58**, No. 7, 964–977.

Innanen, K. A., 2011, Inversion of the seismic AVF/AVA signatures of highly attenuative targets: Geophysics, **76**, No. 1, R1–R14.

Köhn, D., 2011, Time domain 2D elastic full waveform tomography: Ph.D. thesis, Christian-Albrechts Universität Kiel.

Li, Y., 2006, An empirical method for estimation of anisotropic parameters in clastic rocks: The Leading Edge, **25**, No. 6, 706–711.

Malinverno, A., 2002, Parsimonious bayesian markov chain monte carlo inversion in a nonlinear geophysical problem: Geophysical Journal International, **151**, No. 3, 675–688.

Margrave, G. F., 2013, Q tools: Summary of CREWES software for Q modelling and analysis: the 25th Annual Report of the CREWES Project.

Mavko, G., and Jizba, D., 1991, Estimating grain-scale fluid effects on velocity dispersion in rocks: Geophysics, **56**, No. 12, 1940–1949.

Moradi, S., and Innanen, K. A., 2015, Scattering of homogeneous and inhomogeneous seismic waves in low-loss viscoelastic media: Geophysical Journal International, **202**, No. 3, 1722–1732.

Moradi, S., and Innanen, K. A., 2016, Viscoelastic amplitude variation with offset equations with account taken of jumps in attenuation angle: Geophysics, **81**, No. 3, N17–N29.

Moradi, S., and Innanen, K. A., 2017, Born scattering and inversion sensitivities in viscoelastic transversely isotropic media: Geophysical Journal International, **211**, No. 2, 1177–1188.

Müller, T. M., Gurevich, B., and Lebedev, M., 2010, Seismic wave attenuation and dispersion resulting from wave-induced flow in porous rocks—A review: Geophysics, **75**, No. 5, 75A147–75A164.

Pan, W., Innanen, K. A., Margrave, G. F., Fehler, M. C., Fang, X., and Li, J., 2016, Estimation of elastic constants for HTI media using Gauss-Newton and full-Newton multiparameter full-waveform inversion: Geophysics, **81**, No. 5, R275–R291.

Rüger, A., 1998, Reflection coefficients and azimuthal AVO analysis in anisotropic media.: Ph.D. thesis, Colorado School of Mines.

Rüger, A., and Tsvankin, I., 1997, Using AVO for fracture detection: Analytic basis and practical solutions: The Leading Edge, **16**, No. 10, 1429–1434.

Schoenberg, M., and Protazio, J., 1990, ′Zoeppritz′ rationalized, and generalized to anisotropic media: The Journal of the Acoustical Society of America, **88**, No. S1, S46–S46.

Shaw, R. K., and Sen, M. K., 2004, Born integral, stationary phase and linearized reflection coefficients in weak anisotropic media: Geophysical Journal International, **158**, No. 1, 225–238.

Shaw, R. K., and Sen, M. K., 2006, Use of AVOA data to estimate fluid indicator in a vertically fractured medium: Geophysics, **71**, No. 3, C15–C24.

Thomsen, L., 1986, Weak elastic anisotropy: Geophysics, **51**, No. 10, 1954–1966.

Tsvankin, I., 1996, P-wave signatures and notation for transversely isotropic media: An overview: Geophysics, **61**, No. 2, 467–483.

Tsvankin, I., 1997, Reflection moveout and parameter estimation for horizontal transverse isotropy: Geophysics, **62**, No. 2, 614–629.

Whitcombe, D. N., 2002, Elastic impedance normalization: Geophysics, **67**, No. 1, 60–62.